Materials Characterization 175 (2021) 111050

Contents lists available at ScienceDirect

Materials Characterization

journal homepage: www.elsevier.com/locate/matchar

# Twinning characteristics in rolled AZ31B magnesium alloy under three stress states

Luiz Carneiro [a], Duke Culbertson [a], Xianyun Zhu [a,b], Qin Yu [a,*,1], Yanyao Jiang [a,*]

[a] University of Nevada, Reno, Department of Mechanical Engineering, NV 89557, USA
[b] Light Alloy Research Institute, Central South University, Changsha 410012, China

ARTICLE INFO

*Keywords:*
Magnesium alloy
Twinning
Non-basal slips
Strain hardening
Stress state

ABSTRACT

Stress-strain responses and twinning characteristics are studied for a rolled AZ31B magnesium alloy under three different stress states: tension along the normal direction (NDT), compression along the rolled direction (RDC), and torsion about the normal direction (NDTOR) using companion specimens interrupted at incremental strain levels. Tension twinning is extensively induced in twinning-favorable NDT and RDC. All the six variants of tension twin are activated under NDT, whereas a maximum of four variants is activated under RDC. Under NDTOR, both tension twins and compression twins are activated at relatively large strains and twinning occurs in a small fraction of favored grains rather than in the majority of grains. Secondary and tertiary twins are observed in the favorably-orientated grains at high strain levels. Deformation under each stress state shows three stages of strain hardening rate: fast decrease (Stage I), sequential increase (Stage II), and progressive decrease (Stage III). The increase in the hardening rate, which is more significant under NDT and RDC as compared to NDTOR, is attributed to the hardening effect of twin boundaries and twinning texture-induced slip activities. The hardening effect of twin boundaries include the dynamic Hall-Petch hardening induced by the multiplication of twin boundaries (TBs) and twin-twin boundaries (TTBs) as well as the hardening effect associated with the energetically unfavorable TTB formation. When the applied plastic strain is larger than 0.05 under NDT and RDC, the tension twin volume fraction is higher than 50%. The twinning-induced texture leads to the activation of non-basal slips mainly in the twinned volume, *i.e.* prismatic slips under NDT and pyramidal slips under RDC. The low work hardening under NDTOR is due to the prevailing basal slips with reduced twinning activities under NDTOR.

## 1. Introduction

Magnesium (Mg) alloys represent an important category of lightweight structural materials mainly accredited to their high specific (*i.e.* density normalized) strength and stiffness [1]. However, the limited number of available slip systems in its hexagonal close pack (*hcp*) structure reduces its formability at room temperature [1–3]. Due to the asymmetric nature of the *hcp* structure, disparate deformation modes are operated in Mg single crystal loaded in different crystal orientations [3–7]. This can lead to a strong texture for wrought Mg alloys. For instance, hot extrusion results in a strong prismatic texture where most of the grains have the *c*-axes perpendicular to the extrusion direction (ED), whereas hot rolling generates a strong basal texture where the *c*-axes are oriented parallel to the normal direction (ND) of the rolled sheet.

Plastic deformation of Mg alloys at room temperature is accommodated by both dislocation slips and twinning. The common available slip systems are basal $\{0001\}\langle 11\bar{2}0\rangle$, prismatic $\{10\bar{1}0\}\langle 11\bar{2}0\rangle$, and second-order pyramidal $\{11\bar{2}2\}\langle 11\bar{2}3\rangle$ slips, among which the second-order pyramidal is the only slip mode capable of accommodating plastic strain along the *c*-axis. However, pyramidal slip is difficult to activate at room temperature because of its high critical resolved shear stress (CRSS) [3]. The common twinning systems in Mg are $\{10\bar{1}2\}\langle\bar{1}011\rangle$ tension twinning and $\{10\bar{1}1\}\langle 10\bar{1}\bar{2}\rangle$ compression twinning which can accommodate plastic deformation along the *c*-axis. Since tension twinning has a much lower CRSS than these of the pyramidal slip and compression twinning at room temperature, it is usually activated to accommodate tension along the *c*-axis.

* Corresponding authors.
*E-mail addresses:* qin.yu.unr@gmail.com (Q. Yu), yjiang@unr.edu (Y. Jiang).
[1] Current address: Materials Sciences Division, Lawrence Berkeley National Laboratory, Berkeley, CA, 94720, USA.

https://doi.org/10.1016/j.matchar.2021.111050
Received 24 January 2021; Received in revised form 9 March 2021; Accepted 12 March 2021
Available online 17 March 2021

The role of twinning in plastic deformation of Mg alloys has been extensively studied under uniaxial tension and compression [8–17]. The major findings can be summarized into the following categories: (i) accommodation of plastic strain, with an association of a stress relaxation effect [11,14]; (ii) hardening effect due to the generation of twin boundaries *via* a dynamic Hall-Petch mechanism [15,18–21]; (iii) change in the dislocation slip activity due to the twinning-induced deformation texture [15,22]; and (iv) hardening effect due to the generation of energetically unfavorable twin-twin boundaries [8,16,17,23,24]. Other than uniaxial tension or compression, mechanical responses of Mg alloys were also studied under simple shear [9,25,26] and torsion [27–40]. Numerical simulations have shown that the plastic deformation is mostly accommodated by basal slips, prismatic slips, and tension twinning when extruded Mg alloys are subjected to free-end torsion [28], whereas basal slip and tension twinning prevail during torsion about the ND of rolled Mg alloys plate [37]. Furthermore, a recent study shows that tension twins, compression twins, and double twins can be activated under free-end torsion about the ND of a rolled AZ31B plate [32].

From the existing studies mentioned above, the twin characteristics, including twin variant selection, morphology, twin volume fraction (TVF), and twinning-induced texture, are revealed as functions of specific stress state with respect to the texture of the Mg alloys [11,41–43]. However, the twinning characteristics produced under different stress states are difficult to be compared simply because the microstructure of the Mg alloys in different studies is varied to a large extent. In fact, a comparison of the twin structures produced under different stress states is of important significance as it can provide an experimental benchmark to aid the microstructure design of Mg alloys in terms of generating favorable twin structures by pre-straining. For instance, twinning structures and twinning texture play an important role on enhancing mechanical properties of Mg alloys during equal channel angular extrusion (ECAE) [44–46] and high-pressure torsion [47,48], where multiaxial stress states is induced. As such, loading conditions under three stress states that are commonly used to generate twin structures are applied in the current study to the same material, a rolled AZ31B Mg alloy. A detailed comparison of twin structures produced under the three stress states, *i.e.* tension along the ND, compression along the rolled direction (RD), and torsion about the ND, is carried out. Specifically, characterization of the twin structures at incremental strain levels is presented in terms of the twinning morphology, twin boundaries, and twinning-induced texture, as well as their corresponding roles in the deformation responses. In parallel, numerical simulations using an elastic-viscoplastic self-consistent (EVPSC) model are conducted to understand the synergy between different deformation mechanisms under the three stress states.

## 2. Experimental procedure

### 2.1. Material and specimen

The material used in this work is AZ31B (Mg-3Al-1Zn) Mg alloy in the form of a 76.2 mm thickness hot-rolled plate. The original microstructure was analyzed on three orthotropic planes with their normal orientations in the rolled direction (RD), transverse direction (TD), and normal direction (ND) of the plate, respectively. Electron backscattered diffraction (EBSD) scans show that the microstructure is composed by mostly equiaxed grains with an average grain size of approximately 50 μm without showing apparent initial twins (Fig. 1a). The material displays a strong basal texture where most of the grains are oriented with the *c*-axes approximately parallel to the ND.

Dog-bone shaped testing specimens are designed specifically for three loading conditions, *i.e.* tension along the ND (NDT), compression along the RD (RDC), and free-end torsion about the ND (NDTOR), as illustrated in Fig. 1b. The tension specimens are machined along the ND and have a solid cross-section with a 14 mm gage length in an 8 mm diameter. The compression specimens have identical dimensions to the tension specimens, but they are machined with the loading axes parallel to the RD. Tubular specimens are machined with their rotation axes along the ND. The gage section of the tubular specimens has a length of 26 mm with a 24 mm outer diameter and a 20 mm inner diameter. The outside surface of the gage section of each specimen was polished prior to testing using *SiC* sandpapers with grit sizes from P400 to P1000.

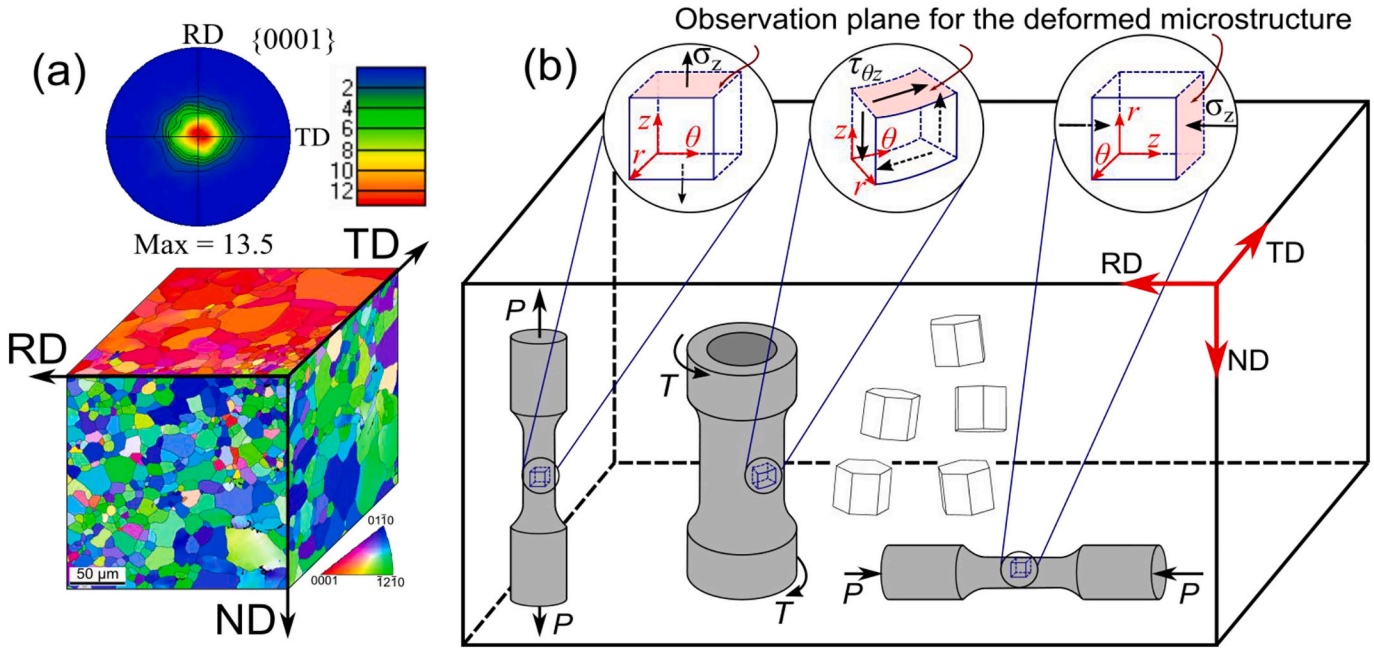


**Fig. 1.** Material and specimens. (a) Three-dimensional EBSD stereograph of the initial microstructure. (b) Schematic illustration of the rolled AZ31B plate with tension and torsion specimens oriented parallel to the ND, while compression specimens oriented parallel to the RD.

### 2.2. Mechanical experiments

Mechanical experiments were performed using a servo-hydraulic axial-torsion Instron fatigue testing machine in ambient air. The machine has an axial load capacity of ±222 kN and torsion load capacity of ±2800 Nm. For the tension and compression experiments, a clip-on extensometer with a gage length of 12.7 mm and strain range of ±0.40 was used for the strain measurement. For the torsion experiments, a modified MTS extensometer with a gage length of 25.4 mm and a shear strain range of ±0.03 was used. The tension and compression experiments were conducted under strain control at a strain rate of 0.005 $s^{-1}$. Torsion experiments were conducted under rotation angle control at an angle rate of 0.7° $s^{-1}$, which is approximately equivalent to a shear strain rate of 0.005 $s^{-1}$.

For the torsion experiments, the extensometer was removed when the shear strain reached the maximum measurement range at 0.03. After the test was completed and the specimen was unloaded, a residual plastic shear strain was measured based on the deformation angle formed between the tangential and axial lines engraved on the outer surface of the specimen before the experiment. The shear strain after the extensometer removal was extrapolated assuming a linear relationship between the shear strain and the rotation angle measured by the rotary variable displacement transducer (RVDT). The shear stress ($\tau$) and the shear strain ($\gamma$) reported are the values calculated on the mid-section of the tubular specimen assuming linear distributions of the shear stress and the shear strain along the thickness of the specimen. To facilitate a comparison among the tension, compression, and torsion loading conditions, the results are presented in terms of the equivalent stress ($\bar{\sigma}$) and equivalent plastic strain ($\bar{\varepsilon}_p$), calculated as.

$$\bar{\sigma} = \sqrt{\sigma^2 + 3\tau^2} \tag{1}$$

$$\bar{\varepsilon}_p = \sqrt{\varepsilon_p^2 + \left(\frac{1}{3}\right)\gamma_p^2} \tag{2}$$

where $\sigma$ is the true axial stress, $\tau$ is the shear stress, $\varepsilon_p$ is the true plastic axial strain, and $\gamma_p$ is the plastic shear strain. Here the true stress and true strain are presented for tension and compression loading cases. It should be noticed that these definitions for the equivalent stress and equivalent plastic strain are for isotropic materials and are adopted in the current study only to facilitate discussions for the textured Mg alloy.

### 2.3. Microstructural characterization

Microstructure evolution under each loading condition was characterized using companion specimens terminated at different strain levels. For the tension and compression experiments, the specimens were tested up to strains of 0.01, 0.02, 0.04, 0.06, 0.08, and up to fracture (0.11 for NDT and 0.15 for RDC). Free-end torsion experiments were conducted up to rotation angles of 5°, 10°, 20°, 30°, and 43° at fracture. The corresponding equivalent plastic strains are 0.007, 0.017, 0.036, 0.055, 0.077, and 0.105 for NDT, 0.008, 0.018, 0.039, 0.059, 0.078, and 0.144 for RDC, and 0.021, 0.040, 0.075, 0.110, and 0.150 for NDTOR. Cross-section samples for EBSD analysis were cut from the gage section of the tested specimen with the scan plane perpendicular to the axial direction (z) of the testing specimen as shown in Fig. 1b. The samples were mechanically ground using *SiC* sandpapers down to P1200 grit size, followed by vibratory polishing using aluminum oxide with particle size of 0.05 μm and etching with 3% Nital for 5 s. The EBSD scans were taken in a Joel 7100 F field emission scanning electron microscope (SEM) equipped with an Oxford HKL Channel 5 instrument at an acceleration voltage of 20 kV. The working distance was 25 mm, and the step size varied from 0.5 μm to 1.0 μm for large scans of 500×500 $\mu m^2$. High-resolution scans with smaller step sizes down to 0.25 μm were taken to capture delicate twin features on local areas.

The relative twin/slip activities associated with each loading condition were evaluated numerically based on an elastic-viscoplastic self-consistent (EVPSC) model [49–52]. The simulations use the real initial texture obtained by EBSD that is discretized in 1000 grain orientations. The considered deformation modes are {0001}<11$\bar{2}$0> basal slip, $\{10\bar{1}0\}$<11$\bar{2}$0> prismatic slip, $\{11\bar{2}2\}$<11$\bar{2}$3> pyramidal slip, and $\{10\bar{1}2\}$<10$\bar{1}$1> tension twinning. To consider the rate-dependent behavior, the reference strain rate for the slip/twinning system is set to be $\dot{\gamma}_0 = 0.001/s$ with a rate sensitivity $m = 0.05$. The material constants were adjusted so that the predicted stress-strain curves under tension (ND and RD), and compression (ND and RD) agree with the experimental ones to the best extent. The material constants used in the EVPSC-TDT model for the rolled AZ31B Mg alloy are listed in Table 1. The detailed information about the implementation of the EVPSC model for the rolled AZ31B can be found in ref. [52].

## 3. Results and discussion

### 3.1. Mechanical response

The stress-plastic strain ($\bar{\sigma} - \bar{\varepsilon}_p$) curves for the three stress states are presented in Fig. 2. The $\bar{\sigma} - \bar{\varepsilon}_p$ curves of the AZ31B under NDT and RDC display a similar sigmoidal shape typical of twinning-dominated deformation [8,9,53,54]. Under these two loading conditions, the material yields at the same equivalent stress of 74 MPa, and the stress responses remain almost identical for early stages of deformation ($\bar{\varepsilon}_p \leq 0.02$). At higher strains, the stress under NDT rises at a faster rate and the flow stress is slightly higher than that under RDC. When the plastic strain reaches 0.075, the two curves intersect again and the flow stress under compression becomes higher until fracture.

To analyze the strain hardening behavior, the plastic modulus ($d\bar{\sigma}/d\bar{\varepsilon}_p$) as a function of $\bar{\varepsilon}_p$ for each loading condition is also presented in Fig. 2. For $\bar{\varepsilon}_p \leq 0.055$, the plastic modulus under NDT is higher than that under RDC. After this point, the plastic modulus under RDC increases at a much faster rate than that under NDT, reaching a maximum of 5.8 GPa at $\bar{\varepsilon}_p = 0.071$ for the former, *v.s.* 3.6 GPa at $\bar{\varepsilon}_p = 0.076$ for the latter. As the strain increases further, the plastic modulus decreases until fracture for both NDT and RDC.

Under NDTOR, the material yields at 59 MPa and the stress-plastic strain curve displays a subtle sigmoidal shape throughout the entire deformation with the equivalent stress constantly lower than those from the other two loading conditions, reaching the maximum value of 193 MPa at fracture. Similarly, the equivalent plastic modulus under torsion is also lower, reaching a maximum of 1.1 GPa at $\bar{\varepsilon}_p = 0.08$. However, the equivalent plastic fracture strain of AZ31B is the largest under NDTOR, reaching $\bar{\varepsilon}_{pf} = 0.15$, a value 4.2% higher than that under RDC and 43% higher than that under NDT.

**Table 1**
Material constants used in EVPSC-TDT model for the rolled AZ31B Mg alloy.

| Mode | $\tau_0$ | $\tau_1$ | $h_0$ | $h_1$ | $h^{i1}$ | $h^{i2}$ | $h^{i3}$ | $h^{i4}$ | $A_1$ | $A_2$ |
|---|---|---|---|---|---|---|---|---|---|---|
| Basal | 15 | 5 | 10 | 0 | 1.0 | 1.0 | 1.0 | 1.0 | | |
| Prismatic | 80 | 60 | 600 | 0 | 1.0 | 1.0 | 1.0 | 1.1 | | |
| Pyramidal | 100 | 95 | 1000 | 0 | 1.0 | 1.2 | 1.0 | 1.25 | | |
| Tension twin | 30 | 20 | 50 | 50 | 2.0 | 1.8 | 1.0 | 1.0 | 0.7 | 0.95 |

### 3.2. Microstructure evolution

#### 3.2.1. Schmid factor analysis for twinning favorability

To facilitate discussion of twin structures, the twinning favorability is analyzed by plotting the generalized Schmid factor (SF) pole figures for each loading condition, as shown in Fig. 3. For a given loading condition, the theoretical maximum SFs are calculated for $\{10\bar{1}2\}<10\bar{1}1>$ tension twin and $\{10\bar{1}1\}<10\bar{1}2>$ compression twin in all possible crystal orientations and projected in the (0001) pole figures. The generalized SFs under NDTOR are calculated as the ratio of the resolved shear stress in a twin system to the external shear stress induced by free-end torsion. Superimposed in the SF pole figures are the projections of the actual crystal orientations (black dots) in the undeformed AZ31B plate. Note that the normal stress $\sigma_z$ and the shear stress $\tau_{\theta z}$ are described in the local coordinates radial ($r$), tangential ($\theta$), and axial ($z$) and the pole figures are presented on the $r$-$\theta$ plane. Under NDT (Fig. 3a), the SFs for tension twinning are the highest near the center of the (0001) pole figure ($c$-axes of the grains almost parallel to the tension direction ($z$)), *vice versa* for compression twinning. Under RDC (Fig. 3b), the highest SFs of tension twinning fall in the region near the edges of the (0001) pole figure ($c$-axes of the grains almost perpendicular to the compression direction ($z$)). For the AZ31B under NDT and RDC, most of the grain orientations (black dots) possess high tension twin SFs, which means that tension twinning is favored.

Under NDTOR, due to the existence of multiaxial stress state, the SF pole figures are not symmetrical such as in the cases of NDT and RDC. Under torsion, a misalignment of the $c$-axis about the $r$-axis by positive or negative rotation may induce twinning SFs of opposite sign. For instance, a grain slightly misaligned towards negative $\theta$-axis, such as Grain A in Fig. 3c, leads to low or negative SF for tension twinning, whereas a slight misalignment towards the positive $\theta$-axis, such as Grain B, results in positive SF for tension twinning. The same rule applies to compression twinning. The original AZ31B basal texture presented in Fig. 3c (black dots) indicates that approximately 70% of the grains have positive tension twinning SF values and remaining 30% grains have negative SFs for tension twinning and high SFs for compression twinning. As a result, both tension and compression twinning can occur under NDTOR.

#### 3.2.2. Twin structure evolution

The microstructure development of AZ31B was analyzed by means of

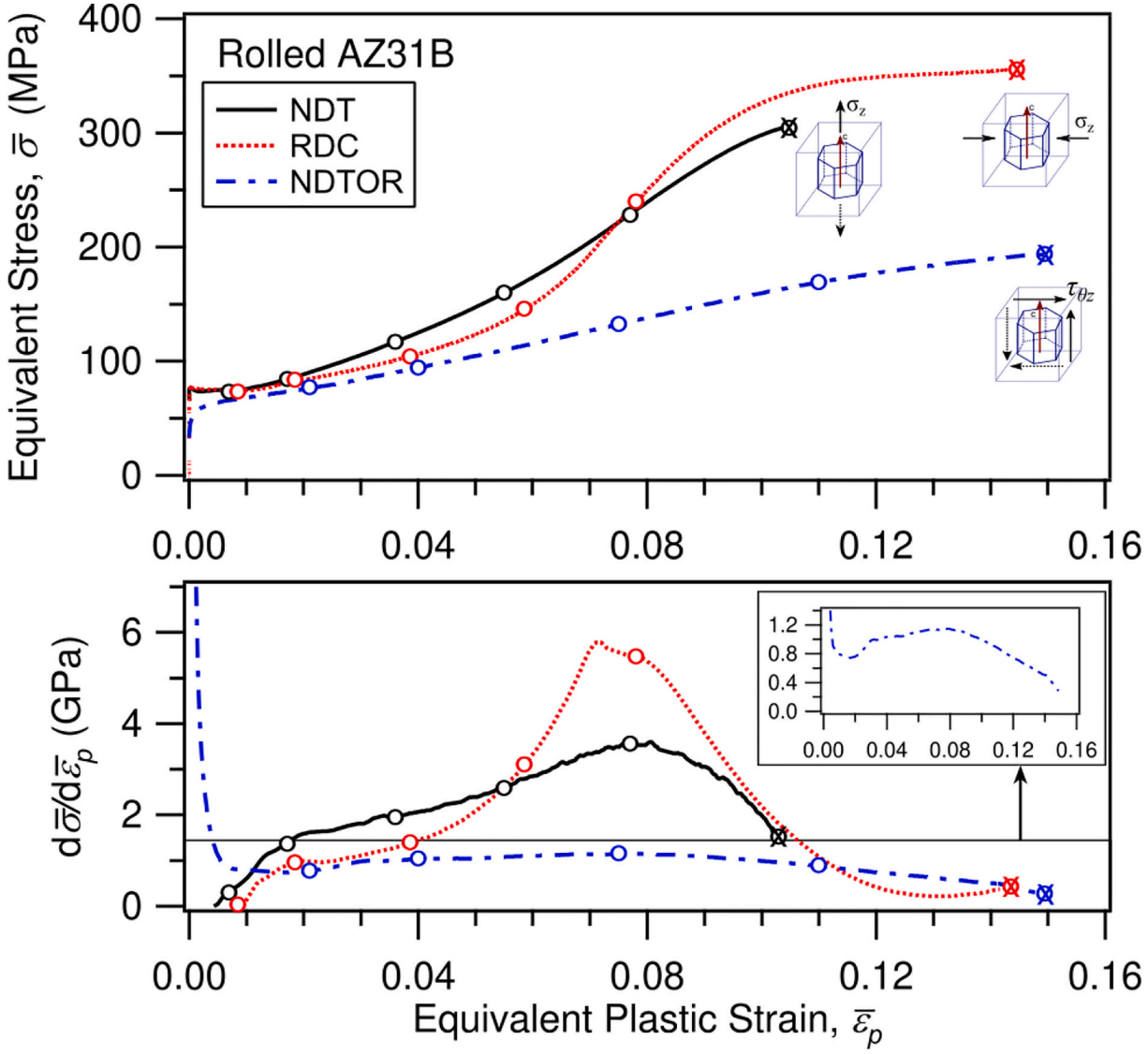


**Fig. 2.** Stress-plastic strain ($\bar{\sigma} - \bar{\varepsilon}_p$) curves and strain hardening rate ($d\bar{\sigma}/d\bar{\varepsilon}_p$) for the rolled AZ31B under NDT, RDC, and NDTOR. White circles denote deformation levels where microstructures were analyzed, and "x" indicates fracture.

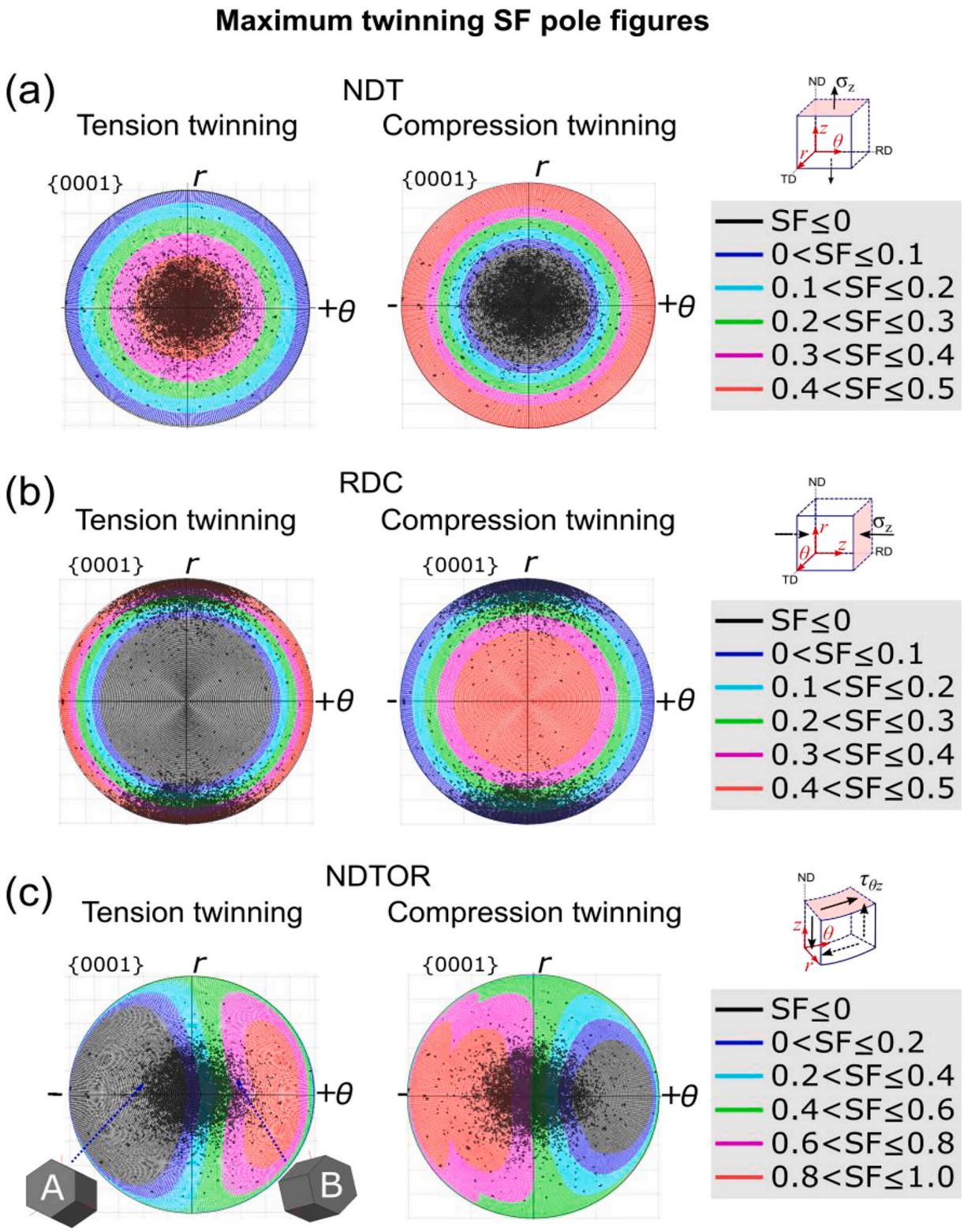


**Fig. 3.** Maximum twinning SF pole figures under the three stress states. Dark dots represent the real orientation of the initial rolled AZ31B.

EBSD and the results for the three loading conditions are compared at similar equivalent plastic strain levels. For each EBSD scan, the inverse pole figure (IPF), band contrast (BC) with twin boundaries (TB) of different types, and the (0001) contour pole figure are presented. Moreover, a depicted grain from each IPF and BC images is analyzed in terms of the twin variants activated. The symbols $T_i$ ($i$ = 1–6) represent the individual $\{10\bar{1}2\}$ twin variant, following the label convention in Ref. [16] where $T_1$ corresponds to the $\left(10\bar{1}2\right)\left[\bar{1}011\right]$ variant, while increasing subscripts correspond to the other variants by a counter-clockwise rotation about the $c$-axis. The symbol $C_i$ (i = 1–6) correspond to the $\{10\bar{1}2\}$ compression twin variant, following the same labeling notation as for tension twinning. Secondary and tertiary twins are represented by the individual twin variants in the sequence of

activation. For instance, $T_i$-$C_j$ means a tension-compression double twin, where a secondary compression twin $C_j$ is formed inside the primary tension twin $T_i$. The types of twin boundaries highlighted in the BC maps include primary tension TB (86° ± 5°<1$\bar{2}$10>), primary compression TB (56° ± 5°<1$\bar{2}$10>), and secondary compression-tension TB (37.5° ± 5°<1$\bar{2}$10>). The twin-twin boundaries (TTB) are also highlighted, including non-co-zone TTB (60° ± 5°<10$\bar{1}$0>), and co-zone TTB (7.4° ± 5°<1$\bar{2}$10>). The twin volume fraction (TVF) was calculated as the ratio of the total area of twins to the total scanned area.

At a low equivalent plastic strain (0.007 for tension and 0.008 for compression), twins can be detected, and the TVF is measured as 5% and 11% under NDT and RDC, respectively. This suggests that twinning is directly related to micro-yielding of AZ31B [11]. Since tension twinning requires a low CRSS to activate, it provides easy accommodation of plastic strain under tension along the *c*-axis or compression perpendicular to the *c*-axis, reducing the work hardening rate [11,14]. Although micro-yielding occurs at the same equivalent stress under NDT and RDC, the lower strain hardening rate under RDC at this plastic strain is speculated to be related to the faster twinning rate and higher TVF.

Fig. 4 shows the microstructure deformed up to equivalent plastic strains of 0.017, 0.019, and 0.021 under NDT, RDC, and NDTOR, respectively. Several grains present at least one twin variant under NDT and RDC, and very few twins are nucleated under NDTOR. The twin

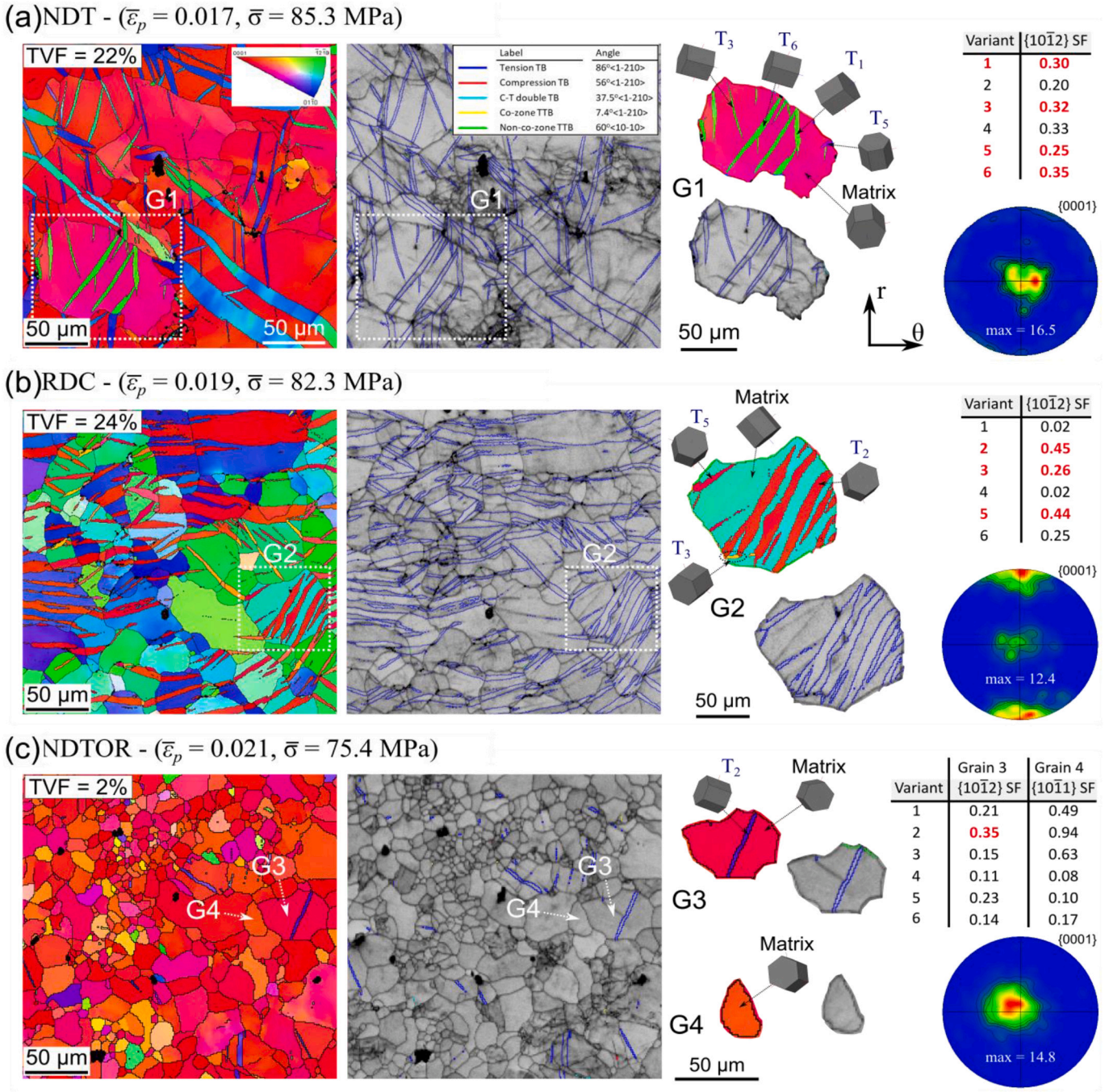


**Fig. 4.** EBSD IPF maps, BC maps, and pole figures of the AZ31B after an equivalent plastic strain of approximately 0.02 under NDT, RDC, and NDTOR. The twin variants with SF in red bold text are activated. (For interpretation of the references to colour in this figure legend, the reader is referred to the web version of this article.)

volume fractions (TVFs) are 22%, 24%, and 2% under NDT, RDC, and NDTOR, respectively. Although tension twinning is equally favorable under tension along the *c*-axis and under compression perpendicular to the *c*-axis, the twinning characteristics, such as active twin variants, twin morphology, and twin texture, are different. Under NDT, several twin variants are activated in a grain due to the high SFs of all six possible variants. For instance, grain G1 in Fig. 4a presents four different twin variants activated ($T_1$, $T_3$, $T_5$, and $T_6$), all with $\{10\bar{1}2\}$ SF higher than 0.25. The large number of active variants in a grain produces several twin bands growing at different trace angles and intersecting with each other. It is noticeable that the selection of twin variants does not strictly follow the Schmid law. For instance, Variant 4 has the second highest rank but it is not activated, while Variant 5 is activated having only the fifth highest rank. The reason for this phenomenon may be related to local stress state and possible defects responsible for twin nucleation [55]. Often, the selection of a primary variant requires the least amount of energy to accommodate strain from neighboring grains, such that the selected variant not necessarily has the highest SF rank.

Unlike in the case under NDT, the twin bands grow mostly in a parallel fashion (Fig. 4b) under RDC. This is a consequence of only two to four twin variants having high SF, depending on the grain orientation. Specifically, one can consider a grain with the *c*-axis perfectly oriented perpendicular to the compression direction. If the crystal is compressed perfectly along the $<10\bar{1}0>$ prismatic face (blue grains on the IPF maps), two variants have maximum SF of 0.499 and the other four possible variants have a much lower SF of 0.125. Alternatively, compression perfectly oriented along the $<1\bar{2}10>$ *a*-axis (light green grains on the IPF maps) induce relatively high SF on four variants (0.3742) and zero on the remaining two variants. Compression on any crystal orientation between these two ideal cases results in two variants with very low SFs for tension twinning (<0.1). On the other hand, tension parallel to the *c*-axis induce SF of 0.499 for all six possible variants. Therefore, the number of possible active twin variants under RDC is less as compared to NDT according to the SF criterion. Moreover, the twin variants of the higher SFs under RDC are the ones that share the same $<11\bar{2}0>$ zone axis (co-zone variants) and induce a lattice re-orientation towards the loading direction (RD). Therefore, the twinning texture is limited to most of the grains having the *c*-axes oriented at the RD$\pm$30° as opposed to the case of NDT where the *c*-axes of the twinned grains are randomly distributed on the RD-TD plane due to equal favorability of all variants [11,41]. For instance, grain G2 in Fig. 4b presents only two major co-zone twin variants $T_2$ and $T_5$, each with similar SF of approximately 0.45, while the other variants have a much lower SF. Furthermore, several twin chains are found across the grains under NDT and RDC, a mechanism known as adjoining twin pair (ATP) formation. ATPs occur when a twin crosses the grain boundary between grains that share similar orientation, *i.e.* grains with high compatibility factor [56].

Under NDTOR at a similar equivalent plastic strain, twinning is much less observed (Fig. 4c), following well the SF analysis (Fig. 3c). At an equivalent plastic strain of 0.021, only very few twin variants are nucleated on the grains favorable for tension twinning. For instance, G3 presents only one band of $T_2$ which is the variant with the highest SF. Conversely, several grains unfavorable for tension twinning remain untwined. Although these grains might have high SF for $\{10\bar{1}1\}$ compression twinning, the local stress is not high enough to activate it due to its high CRSS. In Fig. 4c, G4 remains untwinned even with a maximum $\{10\bar{1}1\}$ SF of 0.94. Unlike in the case of uniaxial loading, NDTOR rarely induces ATP formation. This originates from the uniqueness of the pure shear stress state under torsion. Two neighboring grains with *c*-axes slightly misoriented towards opposite directions with respect to the $\theta$-axis may have SFs with different signs, thus limiting the propagation of the twin across the grain boundary.

Fig. 5 shows the microstructure deformed to equivalent plastic strains of 0.036, 0.039, and 0.04 under NDT, RDC, and NDTOR, respectively. At this strain level, at least one twin band is present in almost every grain favorable for tension twinning regardless of the stress state. The TVF reaches 34% under NDT, and 48% under RDC, an increase of 54%, and 100% from the equivalent plastic strains of 0.017, and 0.018, respectively. The higher relative increase in the TVF under RDC, compared to this under NDT, is mainly attributed to the smaller number of twin-twin interactions in a grain, which may inhibit further grow of a twin band [16,57,58]. For instance, under NDT, grain G5 (Fig. 5a) has five out of six possible variants activated, causing significant twin-twin intersections. These interactions impede further twin growth, *e.g.,* $T_6$ and $T_3$ hindered by $T_1$. Similarly, the thickening of $T_1$ might be constrained by $T_3$, $T_6$, and $T_2$. However, under RDC, fewer twin variants enable a relatively unconstrained twin growth. G6 in Fig. 5b contains at least four bands of a single twin variant ($T_5$). The lack of intersecting twin bands enables profuse growth of $T_5$ bands. The preference of more twin-twin interactions under NDT results in a stress concentration at local junctions, leading to the occurrence of individual secondary tension twins, such as $T_1$-$T_4$ in grain G5 (Fig. 5a) [16]. These secondary twin variants are usually not of the highest SF rank but require the least strain accommodation from the primary twin variant due to the local stress states drastically different from that of the external load [55,59–62]. Furthermore, these types of tension-tension double twins are found to be facilitated by twin-twin boundaries between non-co-zone variants [16,55,63,64].

Under NDTOR (Fig. 5c), the TVF at $\bar{\varepsilon}_p = 0.04$ reaches 14%, an increase of 600% from that at $\bar{\varepsilon}_p = 0.021$, mainly because the resolved shear stresses in many grains favorable for tension twinning exceed the CRSS. At this plastic strain level, different variants with high SFs start to develop within one grain. Similar to the case of $\bar{\varepsilon}_p = 0.021$, most of the grains unfavorable for tension twinning remain untwinned. Although these grains may have significantly high SFs, $\{10\bar{1}1\}$ compression twinning does not occur due to high CRSS.

The microstructure of AZ31B at equivalent plastic strains of 0.077 under NDT, 0.078 under RDC, and 0.075 under NDTOR are shown in Fig. 6. These plastic strain levels approximately represent the peak of plastic strain hardening rates for each loading condition (Fig. 2). The peak of strain hardening rate is usually associated with twinning exhaustion under NDT and RDC [13,53,65,66], with TVF reaching 78% and 85%, respectively. The growth of twins at this strain level furthers twin-twin interactions, as evidenced by the increase in the twin-twin boundaries (green and yellow colour) in the BC maps (Fig. 6a and b). Under NDT, this leads to an increase in the tension-tension double twins and occurrence of different secondary twin variants, such as $T_2$-$T_4$ and $T_2$-$T_6$ in the primary $T_2$ within grain G9 (Fig. 6a). Similarly, under RDC, some tension-tension double twins in less amount are observed, such as $T_1$-$T_2$ formed in the primary $T_1$ in grain G10 (Fig. 6b). Also, the extensive growth of co-zone variants under RDC facilitates the coalescence of the variants such as $T_2$ and $T_5$ in grain G10 (Fig. 6b). Since co-zone twin variants have very similar orientations, the coalescence makes it a challenge to differentiate these co-zone variants.

Under NDTOR at $\bar{\varepsilon}_p = 0.075$, the TVF reaches 21%, an increase of 50% compared to the plastic strain level of 0.04. The grains favoring tension twinning are heavily occupied by the tension twins with high SF ranks, such as $T_2$, $T_3$, $T_5$, and $T_6$ in G11 (Fig. 6c). In the grains unfavorable for tension twinning, such as G12 (Fig. 6c), the external stress ($\bar{\sigma} = 128.7$ MPa) is large enough to activate compression twin of high SFs, such as $C_2$ and $C_6$. The reorientation of these $\{10\bar{1}1\}$ compression twins facilitates the nucleation of a secondary $\{10\bar{1}2\}$ tension twin that rapidly expands in the primary $\{10\bar{1}1\}$ twin, forming compression-tension double twins, such as $C_2$-T in grain G12 (Fig. 6c). Other instances of compression twins and compression-tension double twins are detected in the BC map (red arrows). It is important to note that, unlike NDT and RDC, AZ31B under NDTOR undergoes substantial

compression-tension double twinning even at a plastic strain of approximately 50% of the fracture strain. This implies that the shear localization accommodated by the compression-tension twin boundaries might not be a controlling factor for the ductility of the material under torsion.

The microstructure of AZ31B deformed up to fracture under each loading condition is shown in Fig. 7. The EBSD scans were taken on the samples cut within the gage sections away from the final fracture surface to avoid any effect of the local stress states induced by the fracture surface. At failure under NDT and RDC, the texture of AZ31B is almost completely rotated by approximately 90 degree because of extensive tension twinning, as evidenced in the pole figures in Fig. 7a and b. Specifically, the twinned texture is characterized by most *c*-axes oriented randomly on the RD-TD plane under NDT (Fig. 7a), whereas the *c*-axes are oriented at RD±30° under RDC due to the favorability of the twin variants that re-orient the *c*-axes of the matrix towards the loading axis [11,41]. The TVF reaches 96% under NDT, and 98% under RDC, and most of the grains are fully consumed by the tension twin variants of high SF ranks, such as grain G13 in Fig. 7a and grain G14 in Fig. 7b.

The microstructure at failure under NDTOR at an equivalent plastic

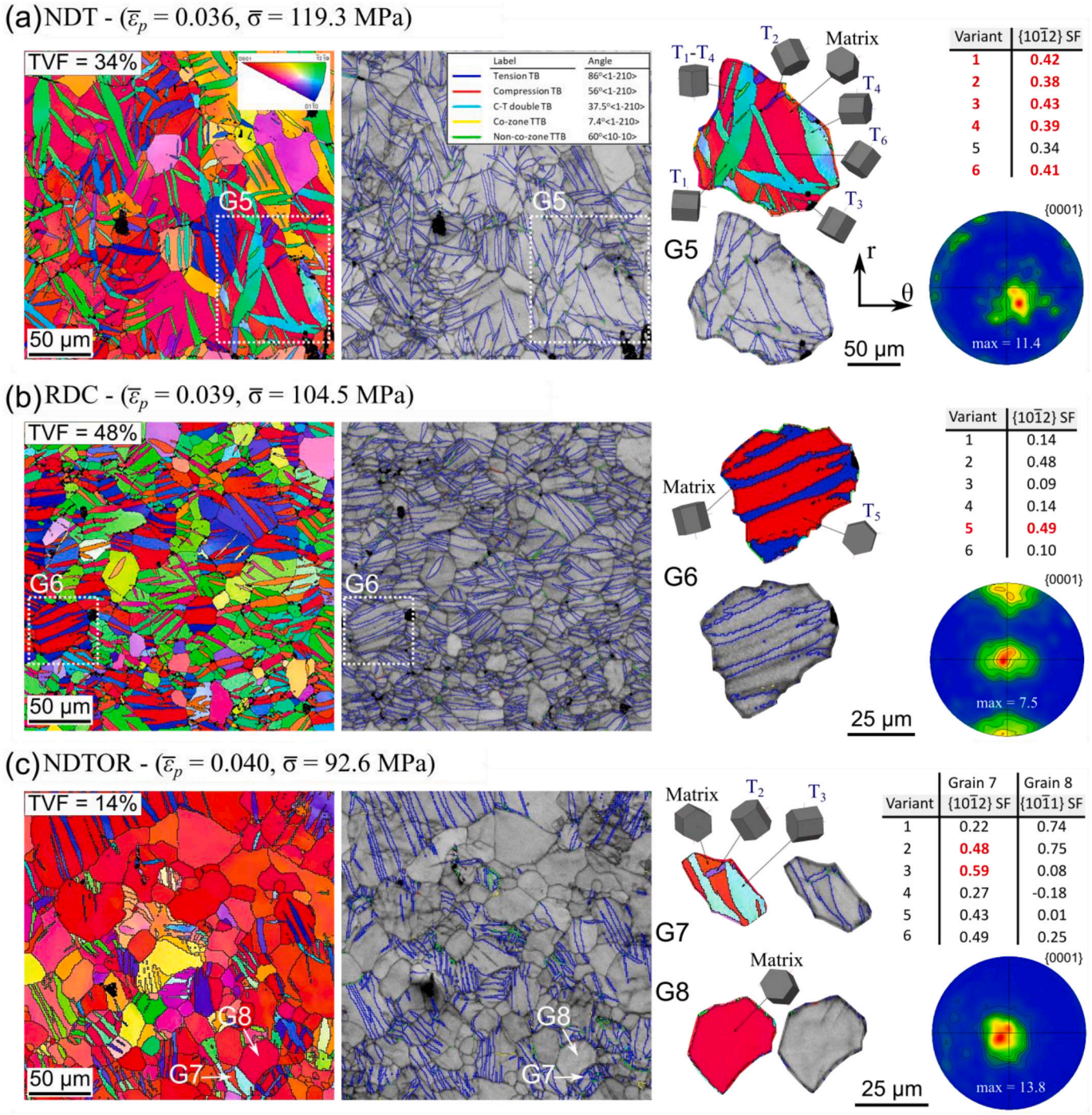


**Fig. 5.** EBSD IPF maps, BC maps, and pole figures of rolled AZ31B after an equivalent plastic strain of approximately 0.04 under NDT, RDC, and NDTOR. The twin variants with SF in red bold text are activated. (For interpretation of the references to colour in this figure legend, the reader is referred to the web version of this article.)

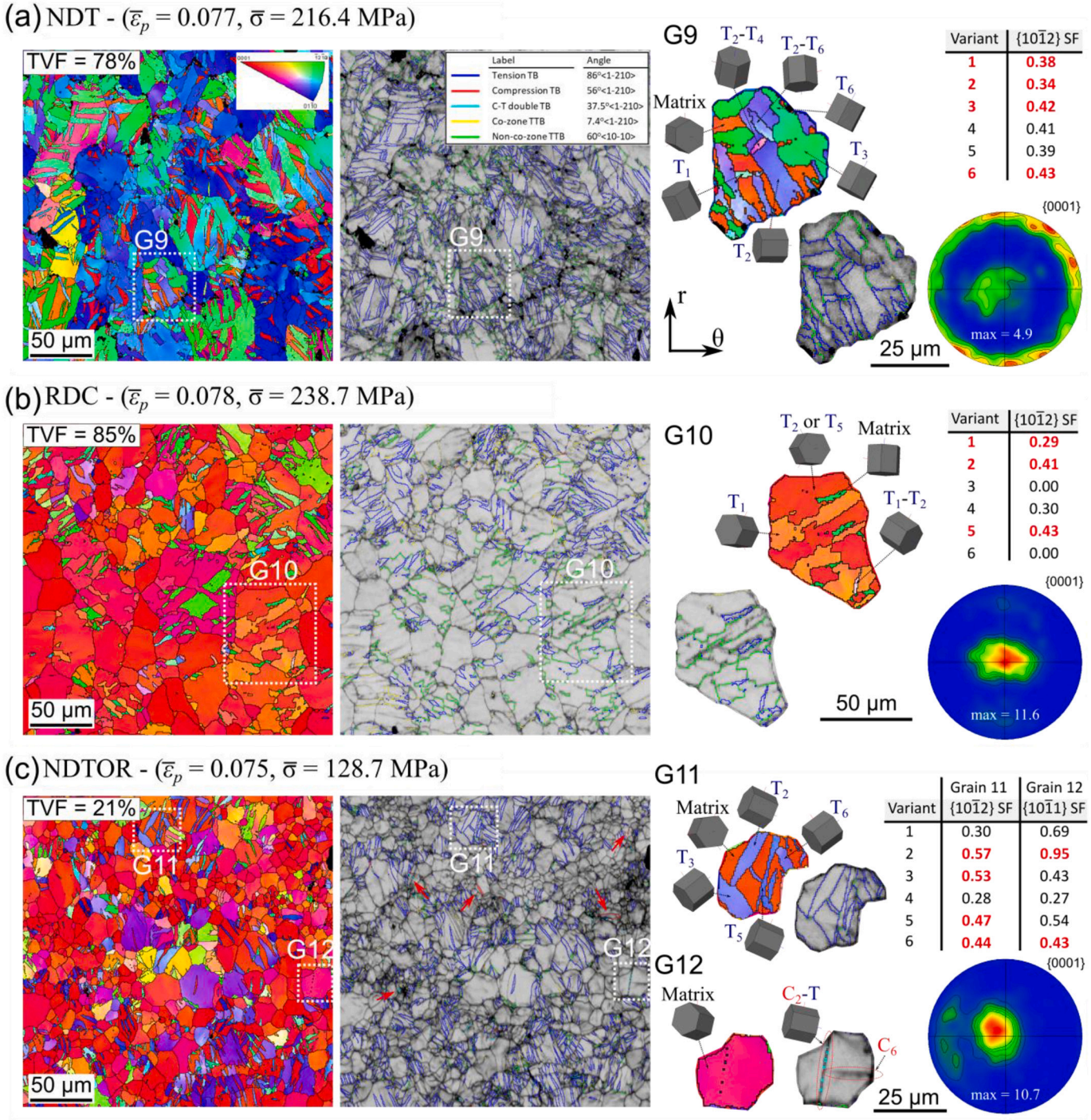


**Fig. 6.** EBSD IPF maps, BC maps, and pole figures of rolled AZ31B after equivalent plastic strains of 0.077, 0.070, and 0.075 under NDT, RDC, and NDTOR, respectively. The twin variants with SF in red bold text are activated. Red arrows in BC map show instances of {10$\bar{1}$1} and {10$\bar{1}$1}-{10$\bar{1}$2} twins. (For interpretation of the references to colour in this figure legend, the reader is referred to the web version of this article.)

strain of 0.15 (Fig. 7c) has a TVF of 44%, which is significantly lower than the cases of NDT and RDC. In those tension-twinned grains, {10$\bar{1}$2}-{10$\bar{1}$1} secondary twins and subsequently {10$\bar{1}$2}-{10$\bar{1}$1}-{10$\bar{1}$2} tertiary twins are observed, such as $T_3$-$C_1$-$T_1$, and $T_3$-$C_4$-$T_2$ in grain G15 (Fig. 7c). The grains unfavorable for tension twinning develop {10$\bar{1}$1}compression twins and subsequential {10$\bar{1}$1}-{10$\bar{1}$2} secondary twins, such as $C_1$-$T_1$, $C_2$-$T_5$, and $C_4$-$T_5$ in grain G16 (Fig. 7c). The sum of the volume fraction of compression twins and compression-tension double twins at failure is approximately 1.1%. Furthermore, micro-cracks are found at the tips of some of these tertiary twins, which implies that the excessive shear localization at the twin boundaries caused by three orders of sequential twinning may be a contributing factor to the fracture of Mg alloys under pure shear.

### 3.3. Roles of twinning in strain hardening rate

It is well established that basal slips and tension twinning play major roles in accommodating plastic deformation at low to intermediate strain levels in strong textured Mg alloys subjected to tension parallel to the *c*-axes [11], compression perpendicular to the *c*-axes [8,11], and

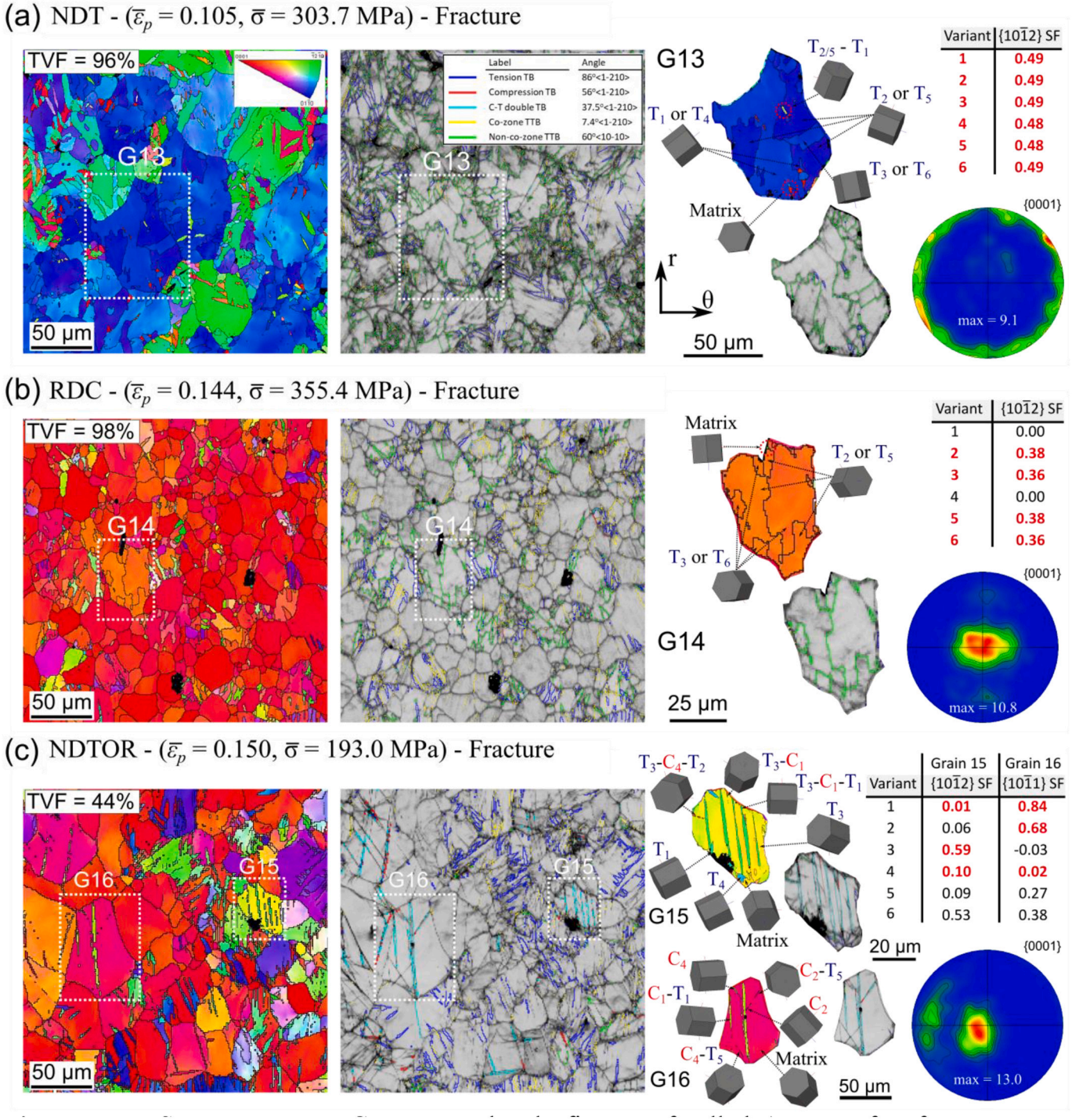


**Fig. 7.** EBSD IPF maps, BC maps, and pole figures of rolled AZ31B after fracture at an equivalent plastic strains of 0.105, 0.144, and 0.15 under NDT, RDC, and NDTOR, respectively. The twin variants with SF in red bold text are activated. (For interpretation of the references to colour in this figure legend, the reader is referred to the web version of this article.)

torsion about the *c*-axes [37]. Because of its low CRSSs, tension twinning directly contributes to the initial yielding under these loading conditions. Abrupt drop and low level of strain hardening rate are always associated with the plastic strain accommodated by twinning due to its stress relaxation effect [11,14,67]. However, twinning can also induce complex hardening effects originated primarily from grain refinement by twin boundaries (known as dynamic Hall-Petch effect) [15,18–21], texture-induced changes in slip activity [11,68], and twin-slip interactions [15,22], and twin-twin interactions [16,17,23].

To clarify and compare the specific roles of twinning in strain hardening in the rolled AZ31B under the three stress states, the length fraction of each type of TB and TTB as a function of the equivalent plastic strain is analyzed. The length fraction of a type of TB or TTB is calculated as the ratio of the total length of that TB or TTB to the sum of all the grain boundaries, TBs, and TTBs. Fig. 8 shows the evolution of each type of TB and TTB under the three loading conditions with respect to the equivalent plastic strain. The twin-related boundaries include primary tension TB (86° ± 5°<1$\bar{2}$10>), primary compression TB (56° ± 5°<1$\bar{2}$10>), and

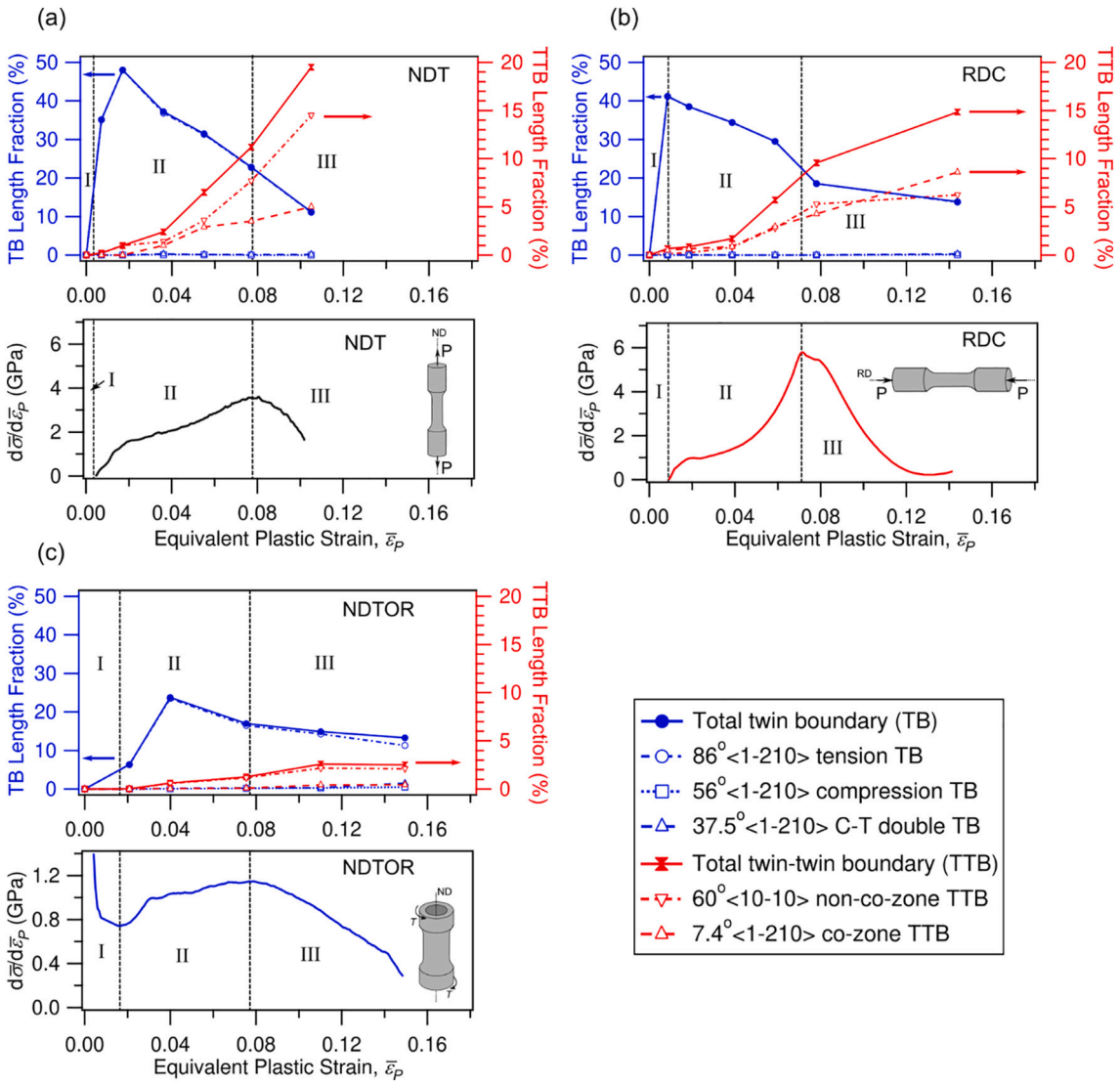


**Fig. 8.** Length fraction of twin boundaries and twin-twin boundaries under (a) NDT, (b) RDC, and (c) NDTOR. The evolution of the plastic modulus is also presented with three distinct stages of plastic strain hardening rate.

secondary compression-tension TB ($37.5° \pm 5°<1\bar{2}10>$), non-co-zone TTB ($60° \pm 5°<10\bar{1}0>$), and co-zone TTB ($7.4° \pm 5°<1\bar{2}10>$). Fig. 8 also presents the evolution of the plastic modulus ($d\bar{\sigma}/d\bar{\varepsilon}_p$) as a function of $\bar{\varepsilon}_p$ for each loading condition. The plastic modulus for each loading condition can be divided into three distinct stages: Stage I – rapid decrease of $d\bar{\sigma}/d\bar{\varepsilon}_p$ attributed to macro-yielding; Stage II – fast resurgence followed by a slower increase of the hardening rate until reaching a maximum; Stage III – continuous decrease of $d\bar{\sigma}/d\bar{\varepsilon}_p$ until fracture. To facilitate the identification of strain hardening stages, the scale used for $d\bar{\sigma}/d\bar{\varepsilon}_p$ under NDTOR (Fig. 8c) is different from those used under NDT and RDC (Fig. 8a and b).

For all the loading conditions, the TB length fraction increases relatively fast in Stage I and at the beginning of Stage II due to the nucleation of tension twins, and then decreases monotonically in Stage III until fracture. The decrease in the TB length fraction is primarily due to the coalescence of twins with the same variant and the expansion of interacted twins with different variants. It is noted here that the tension TB takes most of the total TB length fraction for specimens loaded under NDT and RDC. The length fraction of compression TBs and C-T TBs are only significant under NDTOR, reaching 0.5%, and 1.5%, respectively, at fracture.

The TTB fractions under NDT and RDC increase continuously from Stage II until fracture, whereas under NDTOR, it reaches a plateau at approximately $\bar{\varepsilon}_p = 0.11$. Under NDT, TTBs form at the highest rate due to the high favorability of twin-twin interactions between different variants, and the total TTB fraction reaches 19.5%, whereas under RDC it reaches a maximum of 14.9%, and under NDTOR, 2.5%. It is interesting to find that a higher length fraction of non-co-zone TTBs than that of co-zone TTBs exists under NDT and under NDTOR. The length fractions of non-co-zone TTBs and co-zone TTBs are 14.5% and 5.0%, under NDT, and 2.1% and 0.4%, under NDTOR, respectively. In contrast, RDC induces co-zone TTB length fraction slightly higher than that of non-co-zone type (8.6% against 6.2%, at fracture, respectively). This is due to a favorability of co-zone twin variants under RDC as evidenced in Figs. 4b, 5b, and 6b.

The distinct stages of the plastic hardening rate can be correlated to the variations of the TB and TTB length fractions. At Stage I, the sudden decrease in the plastic modulus, *i.e.,* macro-yielding, reflects in an increase of the TB length fraction due to the nucleation of tension twins. At this stage, this increase occurs at a much faster rate under NDT and RDC, as compared to NDTOR, indicating that twinning plays a more dominant role in the yielding in these two cases. At Stage II, the increase of the plastic modulus is mostly related to the hardening effect of TBs and TTBs, which reduce the mean free path of dislocations [15,18–20]. The

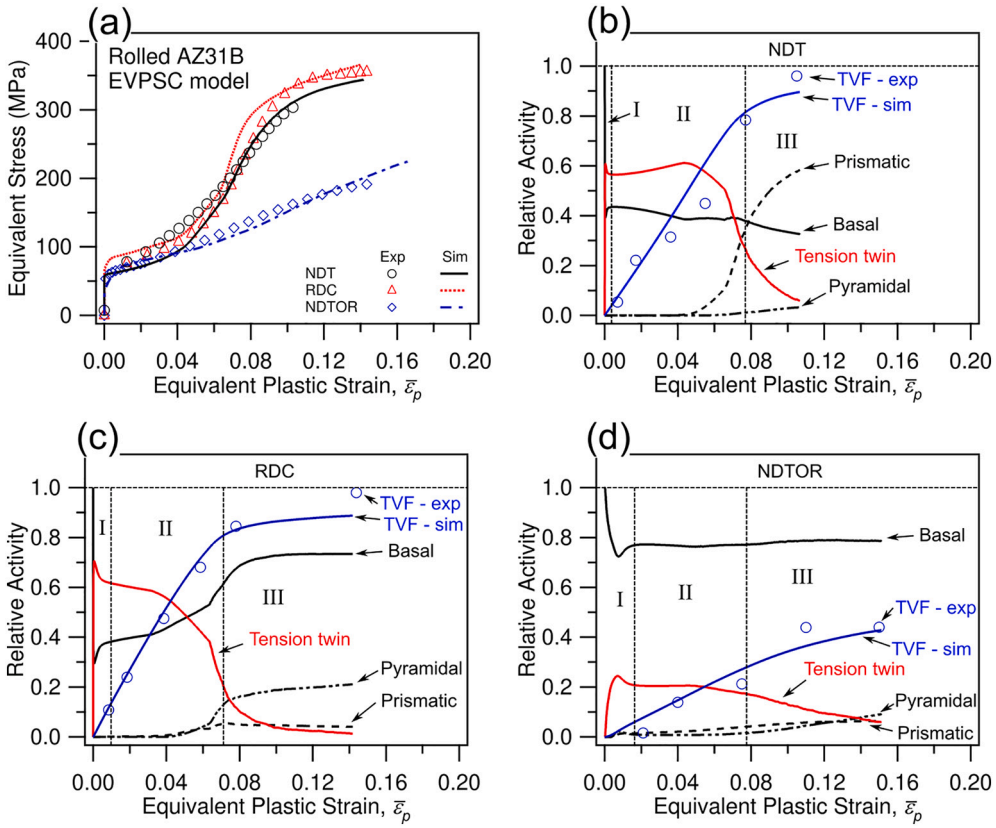


**Fig. 9.** Predicted relative activities of different slip/twinning systems and total TVF under (a) NDT, (b) RDC, and (c) NDTOR. The experimentally measured TVF is also presented.

decreasing TB length fraction with the strain in Stage II indicates a diminishing dynamic Hall-Petch effect. The increasing trend of TTB length fraction continues throughout Stage II, indicating that TTB hardening plays a sustained hardening role. In fact, the work hardening effect of TTBs is not limited to the dynamic Hall-Petch effect, but more significantly, is associated with the additional energy required for their formation, especially for the non-co-zone type [8,16,17,23,24]. This hardening effect contributed by TTB formation is consistent with the much lower hardening rate experienced under NDTOR (Fig. 8c) as compared to those under tension and compression loading condition (Fig. 8a and b).

## 4. Further discussion

The EBSD characterization provides helpful understanding about the influence of twinning on the deformation of Mg alloys. However, an understanding of the roles by different slip systems is feasible by using more advanced characterization techniques such as neutron diffraction [69] or by using plasticity modeling [50]. Here we utilize an elastic visco-plastic self-consistent (EVPSC) model to uncover the activities of various deformation modes associated with the three loading conditions. Fig. 9a presents the simulated equivalent stress-equivalent plastic strain curves obtained by applying the EVPSC model to the rolled AZ31B subjected to NDT, RDC, and NDTOR. The simulated curves show good agreement with the experimental ones. Also, the predicted TVFs in Figs. 9b-9d agree well with the experimentally measured TVF, suggesting that the model parameters used in the simulations can describe well the relative activities of different deformation modes for each loading condition. The relative activities of twin/slip systems predicted by the EVPSC model, including tension twin, as well as basal $<a>$, prismatic $<a>$, and pyramidal $<c+a>$ slip systems, are also presented in Figs. 9b-9d. To interpret the roles of slip/twin activities in the stress-strain responses, the three stages of the plastic strain hardening rate are also overlapped in Figs. 9b-9d.

Under NDT (Fig. 9b), Stage I is characterized by a sharp increase and subsequent small decrease in the relative activity of tension twinning. At the first half of Stage II, twinning activity increases slightly, reaching its maximum of 61% at $\bar{\varepsilon}_p = 0.05$. From this point, the stress is high enough to activate prismatic and pyramidal slips, and their relative activities rise at an increasing rate, reaching 34% and 1% at the end of Stage II, respectively, while tension twinning decreases to 27%. The fast increase of prismatic slip activity is attributed to its lowest CRSS among non-basal slip systems and its high SF in the twinned grains, a phenomenon known as texture-induced slip activity [11]. The increasing operation of prismatic slip promotes plastic deformation and facilitates deformation [70], thus retarding the increase of the hardening rate at the end of Stage II and reducing the strain hardening rate throughout Stage III until failure. At fracture under NDT, the relative activities of basal, prismatic, and pyramidal slips reach 33%, 58%, and 3%, respectively, and the tension twinning activity reaches its minimum at 6% (Fig. 9b).

Under RDC (Fig. 9c), twinning reaches its maximum activity of 70% at the beginning of Stage I. The higher activity of twinning under RDC, compared to that under NDT, delays the increase of strain hardening rate experienced in Stage II. In Stage II, twinning activity decreases at an increasingly rate, accompanied by an increase in basal slip activity. Although prismatic slip has a much lower CRSS as compared to pyramidal, the texture with increasing tension TVF attained by compression favors pyramidal slip operation, causing a faster increase in its relative activity, as compared to prismatic slip. Moreover, the high flow stress attributed to the decreasing twinning activity under RDC facilitates the activation of these pyramidal slips. The favorability of pyramidal slip with a higher CRSS, over the prismatic slips, induces a higher increase in the hardening rate in RDC as compared to NDT. At fracture under RDC,

the relative activities of basal, pyramidal, and prismatic slips reach 73%, 21%, and 4%, respectively, and the tension twinning activity reaches its minimum at 1% (Fig. 9c).

Under NDTOR, basal slips are active throughout the entire loading history (Fig. 9d). After macro-yielding, the twinning activity rises at a much lower rate as compared to the tension/compression loading cases, reaching a maximum of ~24%, while basal slip accounts for the other 76% of the plastic deformation. The slower twinning activation promotes a much smoother transition from elastic to elastic-plastic deformation observed in the stress-plastic strain curve and the plastic modulus in Fig. 2. In Stage II, the tension twinning activity decreases at an almost constant rate, while prismatic slip activity increases from the very beginning of Stage II, and continues to rise through Stage III, when pyramidal slips are also activated. Meanwhile, basal slip activity increases at a steady rate, dominating deformation until fracture. At the end of Stage III, basal, prismatic, and pyramidal slip activities reach 79%, 6%, and 9%, respectively, whereas tension twin reaches 6%. The modest rise in the hardening rate at Stage II under torsion is mostly attributed to the reduced hardening effects related to twinning, as discussed in Section 0. It is worthy to note that under NDTOR both the matrix and the twinned regions are favorable for basal slips which promote plastic-strain accommodation but contribute to less hardening as compared to NDT and RDC.

The different stress responses of AZ31B under different stress states with respect to the texture of the material, as shown in Fig. 2, can be explained based on the inherent differences in the twinning and non-basal slip behavior. The microstructure evolution presented in Figs. 4-7 show that each stress state induces unique twinning features, such as TVF, TB and TTB fractions, and texture. Although tension twinning facilitates plastic deformation, the barrier effects on dislocation motion of TBs and TTBs of different types (Fig. 8) contribute to the increase of strain hardening rate. In terms of slip activity, the operation of non-basal slip systems as the strain increases is dependent on the twinning-induced texture. For instance, the texture induced by NDT promotes high SFs for prismatic slips in the twinned grains, whereas RDC favors the operation of pyramidal slips (Fig. 8). The distinct work hardening contributed by various TBs and non-basal slips leads to the observed different strain hardening rates of AZ31B under different stress states.

## 5. Conclusions

A rolled AZ31B Mg alloy was deformed monotonically under three stress states: tension along ND (NDT), compression along RD (RDC), and torsion about ND (NDTOR). For each loading condition, the evolution of twin structure was characterized using companion specimens deformed at different plastic strains. Additionally, simulations using an EVPSC model were applied to reveal the relative activity of distinct deformation modes. The stress-strain response and the microstructure evolution as a function of increasing strain were studied in detail with a focus on the understanding of the role of deformation twinning in the mechanical behavior of AZ31B. The following conclusions can be made.

1. The stress-strain curves show a strong sigmoidal shape under NDT and RDC due to extensive activation of twinning, whereas under NDTOR the sigmoidal shape of the stress-strain curve is subtle due to less significant role of twinning as a deformation mode. The shape of the stress-strain curve is associated with three different stages of strain hardening rate: fast decrease due to macroscopic yielding (Stage I), sequential increase (Stage II), and progressive decrease (Stage III). The equivalent strain at failure is the maximum under NDTOR, followed by RDC and NDT.
2. Tension twinning is extensively induced under NDT and RDC. With increasing strain under NDT, tension twins of all six variants dominate the microstructure, whereas under RDC the number of variants is limited up to a maximum of four. Under NDTOR, multiple tension twins are observed in the grains favorable for tension twinning following the SF criterion. In these grains, multiple T-C double and T-C-T tertiary twins are detected at a strain of approximately 50% of the fracture strain. The grains unfavorable for tension twin produce extensive compression twin and C-T double twins at large strains.
3. The observed increase in strain hardening rate with applied strain during Stage II can be ascribed to the twinning texture-induced slip activities and dynamic Hall-Petch hardening effect of inhibiting dislocation motion induced by the multiplication of TB and TTB, along with the hardening effect associated with the energetically unfavorable TTB formation. The higher length fraction of TBs and TTBs under NDT and RDC are responsible for the faster increasing in hardening rates as compared to NDTOR.
4. With an applied plastic strain larger than 0.05 under NDT and RDC, the tension twin volume fraction is higher than 50%. The twinning-induced texture in NDT leads to the activation of non-basal prismatic slips at intermediate strains, whereas the texture in RDC favors pyramidal slips, which results in a higher hardening rate due to the higher CRSS of pyramidal slips.
5. Under NDTOR, basal slips and twinning accommodate the plastic strain throughout all the deformation stages, which leads to much lower hardening rate as compared to NDT and RDC.

## Data availability

The raw/processed data required to reproduce these findings cannot be shared at this time due to technical or time limitations.

## Declaration of Competing Interest

The authors declare that the research was conducted in the absence of any commercial or financial relationships that could be construed as a potential conflict of interest.

## Acknowledgments

The research was supported by the U.S. National Science Foundation (CMMI-1762312). X. Zhu gratefully acknowledges the support of China Scholarship Council (CSC).

## References

[1] I.J. Polmear, Magnesium alloys and applications, Mater. Sci. Technol. 10 (2012) 1–16.
[2] M. Barnett, Influence of deformation conditions and texture on the high temperature flow stress of magnesium AZ31, J. Light. Met. 1 (2001) 167–177.
[3] B.C. Wonsiewicz, A. Backofen, Plasticity of magnesium crystals, Trans. Metall. Soc. AIME 239 (1967) 1422–1431.
[4] Y. Hideo, H. Ryo, Deformation mechanisms in magnesium single crystals compressed in the direction parallel to hexagonal axis, Trans Japan Inst Met 4 (1963) 1–8.
[5] B. Syed, J. Geng, R.K. Mishra, et al., Compression response at room temperature of single-crystal magnesium, Scr. Mater. 67 (2012) 700–703.
[6] N.M. Della Ventura, S. Kalácska, D. Casari, et al., {101¯2} twinning mechanism during in situ micro-tensile loading of pure Mg: Role of basal slip and twin-twin interactions, Mater. Des. 197 (2021) 109206.
[7] D. Culbertson, Q. Yu, Y. Jiang, On the intrusion-like co-zone twin-twin structure: an in situ observation, Mater. Lett. 286 (2020) 129140.
[8] L. Jiang, J.J. Jonas, A.A. Luo, et al., Influence of {10−12} extension twinning on the flow behavior of AZ31 Mg alloy, Mater. Sci. Eng. A 445-446 (2007) 302–309.
[9] X.Y. Lou, M. Li, R.K. Boger, et al., Hardening evolution of AZ31B Mg sheet, Int. J. Plast. 23 (2007) 44–86.
[10] C.H. Cáceres, P. Lukác, A. Blake, Strain hardening due to {10-12} twinning in pure magnesium, Philos. Mag. 88 (2008) 991–1003.
[11] S.-G. Hong, S.H. Park, C.S. Lee, Role of {10−12} twinning characteristics in the deformation behavior of a polycrystalline magnesium alloy, Acta Mater. 58 (2010) 5873–5885.
[12] M. Knezevic, A. Levinson, R. Harris, et al., Deformation twinning in AZ31: influence on strain hardening and texture evolution, Acta Mater. 58 (2010) 6230–6242.
[13] M.R. Barnett, Twinning and the ductility of magnesium alloys Part I, tension twins, Mater. Sci. Eng. A 464 (2007) 1–7.
[14] L. Jiang, J.J. Jonas, A.A. Luo, et al., Twinning-induced softening in polycrystalline AM30 Mg alloy at moderate temperatures, Scr. Mater. 54 (2006) 771–775.

[15] F. Wang, S.R. Agnew, Dislocation transmutation by tension twinning in magnesium alloy AZ31, Int. J. Plast. 81 (2016) 63–86.
[16] Q. Yu, J. Wang, Y. Jiang, et al., Twin–twin interactions in magnesium, Acta Mater. 77 (2014) 28–42.
[17] Q. Yu, J. Wang, Y. Jiang, et al., Co-zone {1¯012} twin interaction in magnesium single crystal, Mater Res Lett 2 (2014) 82–88.
[18] S.G. Song, G.T. Gray, Influence of temperature and strain rate on slip and twinning behavior of Zr, Metall Mater Trans A 26 (1995) 2665–2675.
[19] H. El Kadiri, A.L. Oppedal, A crystal plasticity theory for latent hardening by glide twinning through dislocation transmutation and twin accommodation effects, J Mech Phys Solids 58 (2010) 613–624.
[20] A. Serra, D.J. Bacon, R.C. Pond, Twins as barriers to basal slip in hexagonal-close-packed metals, Metall Mater Trans A 33 (2002) 809–812.
[21] A.A. Salem, S.R. Kalidindi, R.D. Doherty, Strain hardening regimes and microstructure evolution during large strain compression of high purity titanium, Scr. Mater. 46 (2002) 419–423.
[22] Z.S. Basinski, M.S. Szczerba, M. Niewczas, et al., The transformation of slip dislocations during twinning of copper-aluminum alloy crystals, La Rev Métallurgie 94 (1997) 1037–1044.
[23] X. Liao, J. Wang, J. Nie, et al., Deformation twinning in hexagonal materials, MRS Bull. 41 (2016) 314–319.
[24] Q. Yu, J. Zhang, Y. Jiang, Direct observation of twinning-detwinning-retwinning on magnesium single crystal subjected to strain-controlled cyclic tension-compression in [0 0 0 1] direction, Philos. Mag. Lett. 91 (2011) 757–765.
[25] J.-Y.Y. Kang, B. Bacroix, R. Brenner, Evolution of microstructure and texture during planar simple shear of magnesium alloy, Scr. Mater. 66 (2012) 654–657.
[26] H. Zhang, G. Huang, L. Wang, et al., Improved ductility of magnesium alloys by a simple shear process followed by annealing, Scr. Mater. 69 (2013) 49–52.
[27] B. Beausir, L.S. Tóth, F. Qods, et al., Texture and mechanical behavior of magnesium during free-end torsion, J Eng Mater Technol Trans ASME 131 (2009) 0111081–01110815.
[28] P.D. Wu, H. Wang, K.W. Neale, On the large strain torsion of HCP polycrystals, Int. J. Appl. Mech. 4 (2012) 1–27.
[29] J. Wang, X.Y. Yang, Y. Li, et al., Enhanced ductility and reduced asymmetry of Mg-2Al-1Zn alloy plate processed by torsion and annealing, Trans. Nonferrous Metals Soc. China 25 (2021) 3928–3935. English Ed 2015.
[30] F. Kabirian, A.S. Khan, T. Gnäupel-Herlod, Visco-plastic modeling of mechanical responses and texture evolution in extruded AZ31 magnesium alloy for various loading conditions, Int. J. Plast. 68 (2015) 1–20.
[31] B. Song, N. Guo, R. Xin, et al., Strengthening and toughening of extruded magnesium alloy rods by combining pre-torsion deformation with subsequent annealing, Mater. Sci. Eng. A 650 (2016) 300–304.
[32] L. Carneiro, D. Culbertson, Q. Yu, et al., Twinning in rolled AZ31B magnesium alloy under free-end torsion, Mater. Sci. Eng. A 801 (2021) 140405.
[33] J. Hu, H. Gao, Y. Meng, et al., Effects of free-end torsion on the microstructure evolution and fatigue properties in an extruded AZ31 rod, Mater. Sci. Eng. A 726 (2018) 215–222.
[34] A.A. Roostaei, H. Jahed, Multiaxial cyclic behaviour and fatigue modelling of AM30 mg alloy extrusion, Int. J. Fatigue 97 (2017) 150–161.
[35] A. Gryguć, S.B. Behravesh, S.K. Shaha, et al., Multiaxial cyclic behaviour of extruded and forged AZ80 mg alloy, Int. J. Fatigue 127 (2019) 324–337.
[36] S. Biswas, B. Beausir, L.S. Toth, et al., Evolution of texture and microstructure during hot torsion of a magnesium alloy, Acta Mater. 61 (2013) 5263–5277.
[37] X.Q. Guo, W. Wu, P.D. Wu, et al., On the swift effect and twinning in a rolled magnesium alloy under free-end torsion, Scr. Mater. 69 (2013) 319–322.
[38] J. Wang, D. Zhang, Y. Li, et al., Effect of initial orientation on the microstructure and mechanical properties of textured AZ31 mg alloy during torsion and annealing, Mater. Des. 86 (2015) 526–535.
[39] B. Song, C. Wang, N. Guo, et al., Improving tensile and compressive properties of an extruded AZ91 rod by the combined use of torsion deformation and aging treatment, Materials (Basel) 10 (2017) 3–8.
[40] N. Guo, B. Song, C. Guo, et al., Improving tensile and compressive properties of magnesium alloy rods via a simple pre-torsion deformation, Mater. Des. 83 (2015) 270–275.
[41] S.H. Park, S.G. Hong, C.S. Lee, Activation mode dependent {10-12} twinning characteristics in a polycrystalline magnesium alloy, Scr. Mater. 62 (2010) 202–205.
[42] S. Godet, L. Jiang, A.A. Luo, et al., Use of Schmid factors to select extension twin variants in extruded magnesium alloy tubes, Scr. Mater. 55 (2006) 1055–1058.
[43] L. Jiang, J.J. Jonas, R.K. Mishra, et al., Twinning and texture development in two mg alloys subjected to loading along three different strain paths, Acta Mater. 55 (2007) 3899–3910.
[44] I.J. Beyerlein, L.S. Tóth, Texture evolution in equal-channel angular extrusion, Prog. Mater. Sci. 54 (2009) 427–510.
[45] B. Beausir, S. Suwas, L.S. Tóth, et al., Analysis of texture evolution in magnesium during equal channel angular extrusion, Acta Mater. 56 (2008) 200–214.
[46] A. Yamashita, Z. Horita, T.G. Langdon, Improving the mechanical properties of magnesium and a magnesium alloy through severe plastic deformation, Mater. Sci. Eng. A 300 (2001) 142–147.
[47] L. Tang, Y. Zhao, N. Liang, et al., Localized deformation via multiple twinning in a mg–Gd–Y–Zr alloy processed by high-pressure torsion, Mater. Sci. Eng. A 677 (2016) 68–75.
[48] S.A. Torbati-Sarraf, S. Sabbaghianrad, R.B. Figueiredo, et al., Orientation imaging microscopy and microhardness in a ZK60 magnesium alloy processed by high-pressure torsion, J. Alloys Compd. 712 (2017) 185–193.
[49] H. Wang, P.D. Wu, C.N. Tomé, et al., A constitutive model of twinning and detwinning for hexagonal close packed polycrystals, Mater. Sci. Eng. A 555 (2012) 93–98.
[50] H. Wang, P.D. Wu, J. Wang, et al., A crystal plasticity model for hexagonal close packed (HCP) crystals including twinning and de-twinning mechanisms, Int. J. Plast. 49 (2013) 36–52.
[51] H. Wang, P.D. Wu, C.N. Tomé, et al., A finite strain elastic-viscoplastic self-consistent model for polycrystalline materials, J Mech Phys Solids 58 (2010) 594–612.
[52] X. Zhu, Y. Wang, L. Carneiro, et al., An experimental evaluation of elastic-viscoplastic self-consistent models for a rolled magnesium alloy under monotonic loading along different material orientations, Submitted to, J Mag Alloys. (2021).
[53] Y.N. Wang, J.C. Huang, The role of twinning and untwinning in yielding behavior in hot-extruded Mg-Al-Zn alloy, Acta Mater. 55 (2007) 897–905.
[54] G. Proust, C.N. Tomé, A. Jain, et al., Modeling the effect of twinning and detwinning during strain-path changes of magnesium alloy AZ31, Int. J. Plast. 25 (2009) 861–880.
[55] S. Mu, J.J. Jonas, G. Gottstein, Variant selection of primary, secondary and tertiary twins in a deformed Mg alloy, Acta Mater. 60 (2012) 2043–2053.
[56] D. Culbertson, Q. Yu, Y. Jiang, In situ observation of cross-grain twin pair formation in pure magnesium, Philos. Mag. Lett. 98 (2018) 139–146.
[57] H. El Kadiri, J. Kapil, A.L. Oppedal, et al., The effect of twin-twin interactions on the nucleation and propagation of {101¯ 2} twinning in magnesium, Acta Mater. 61 (2013) 3549–3563.
[58] M. Gong, S. Xu, Y. Jiang, et al., Structural characteristics of {1¯012} non-cozone twin-twin interactions in magnesium, Acta Mater. 159 (2018) 65–76.
[59] S. Xu, M. Gong, Y. Jiang, et al., Secondary twin variant selection in four types of double twins in titanium, Acta Mater. 152 (2018) 58–76.
[60] H. Qin, J.J. Jonas, Variant selection during secondary and tertiary twinning in pure titanium, Acta Mater. 75 (2014) 198–211.
[61] É. Martin, L. Capolungo, L. Jiang, et al., Variant selection during secondary twinning in mg-3%Al, Acta Mater. 58 (2010) 3970–3983.
[62] M.R. Barnett, Z. Keshavarz, A.G. Beer, et al., Non-Schmid behaviour during secondary twinning in a polycrystalline magnesium alloy, Acta Mater. 56 (2008) 5–15.
[63] A. Jager, A. Ostapovets, P. Molnár, et al., {10-12}-{10-12} double twinning in magnesium, Philos. Mag. Lett. 91 (2011) 537–544.
[64] Z.Z. Shi, Y. Zhang, F. Wagner, et al., Sequential double extension twinning in a magnesium alloy: combined statistical and micromechanical analyses, Acta Mater. 96 (2015) 333–343.
[65] H. Qiao, X.Q. Guo, A.L. Oppedal, et al., Twin-induced hardening in extruded mg alloy AM30, Mater. Sci. Eng. A 687 (2017) 17–27.
[66] P.D. Wu, X.Q. Guo, H. Qiao, et al., On the rapid hardening and exhaustion of twinning in magnesium alloy, Acta Mater. 122 (2017) 369–377.
[67] B. Clausen, C.N. Tomé, D.W. Brown, et al., Reorientation and stress relaxation due to twinning: modeling and experimental characterization for Mg, Acta Mater. 56 (2008) 2456–2468.
[68] S.K. Sahoo, S. Biswas, L.S. Toth, et al., Strain hardening, twinning and texture evolution in magnesium alloy using the all twin variant polycrystal modelling approach, Int. J. Plast. 128 (2020) 102660.
[69] M. Wang, X.Y. Xu, H.Y. Wang, et al., Evolution of dislocation and twin densities in a mg alloy at quasi-static and high strain rates, Acta Mater. 201 (2020) 102–113.
[70] J. Koike, Enhanced deformation mechanisms by anisotropic plasticity in polycrystalline Mg alloys at room temperature, Metall Mater Trans A Phys Metall Mater Sci 36 (2005) 1689–1696.